ESO Science Archive Facility - Phase 3 Data Release Description
ESO programme X-Shooter Spectral Library (XSL), Data Release DR1
provided by S. C. Trager, submitted between 2020-08-25 and 2020-09-25, published on 2020-10-06

XSL DR1 (Phase 3 data)

Abstract

The XSL (X-shooter Spectral Library) project aims to build a new, moderate-resolution stellar spectral library for use in stellar population modelling. Once completed, XSL will represent a significant improvement of current empirical stellar spectral libraries in terms of stellar parameters and wavelength coverage. The survey was conducted in two phases: a two-semester pilot survey and a Large Programme. The pilot survey was undertaken in Periods 84 (084.B-0869) and 85 (085.B-0751) between 1 October 2009 and 30 September 2010. The XSL Large Programme (189.B-0925) was carried out in Periods 89–92 (1 April 2012 – 30 September 2013, with some OBs being finished in P93 until mid March 2014), resulting in spectra of a total of nearly 700 unique stars.

We present the first release (DR1) of the X-shooter Spectral Library (XSL). This release contains 246 observations of 237 stars, spanning the wavelength range of 3000–10200 Å at a resolving power of $R \equiv \lambda / \Delta\lambda \sim 10\,000$. This sample contains multiple observations of some stars, in particular variable cool giants (long-period variables and Mira-type stars) to probe their spectral variability. In the Large Programme a handful of cool giants were observed at multiple epochs to probe spectral variability.

The spectra are flux-calibrated and telluric-corrected. We describe a new technique for the telluric correction. The wavelength coverage, spectral resolution, and spectral type of this library make it well suited to stellar population synthesis of galaxies and clusters, kinematics investigation of stellar systems, and the study of the physics of cool stars.

Overview of Observations

XSL's targets were selected to cover as much of the Hertzsprung–Russell diagram (HRD) as possible. First, we took stars from Lick/IDS, MILES, and NGSL to cover Teff , log(g), and [Fe/H] as uniformly as possible. However, these libraries mostly lack the cool, bright stars, which are important in the NIR. For this purpose, we select AGB and long-period variable (LPV) stars from Lançon & Wood (2000, hereafter LW2000) and IRTF-SpeX with a declination < 35◦ marked M, C or S-stars. LPV stars are also collected from Hughes & Wood (1990, for the Large Magellanic Cloud) and the Cioni et al. (2003, for the Small Magellanic Cloud). Red supergiant stars are taken from the lists of LW2000 and Levesque et al. (2005, 2007). To cover metal-rich stars with abundances similar to giant elliptical galaxies, we also include Galactic Bulge giants from the samples of Blanco et al. (1984) and Groenewegen & Blommaert (2005).

Almost all XSL stars were observed with a narrow slit in nodding mode for improved sky subtraction. Nearly all were also observed in staring mode with a wide slit to derive a narrow slit flux loss correction. Wide-slit observations were carried out (except for the brightest stars, as these would saturate the detectors in that configuration) just before nodding observations. Along with the program stars, we observed hot stars (mostly B-type) to be used as telluric standard stars. These were observed using the same narrow-slit setup to preserve the spectral resolution. Flux standard stars taken as part of the normal ESO X-shooter calibration program were collected from the archive; these were observed using a wide slit (5" × 11") to sample as much of the total flux as possible. Our observing programme was designed to fill any gaps in the observing queue, and therefore the observations were typically taken during poor seeing and thick cloud conditions. This did not however affect the relative flux calibration precision. The observed modes used, slit widths, and CCD readout modes are given in Table 1.

Mode	Arm	Slit	λ (nm)	R	Readout (bright)	Readout (faint)
Nod	UVB	$0\farcs5 \times 11''$	300–600	9100	400k/1pt/hg	100k/1pt/hg
Nod	VIS	$0\farcs7 \times 11''$	600–1020	11 000	400k/1pt/hg	100k/1pt/hg/2 × 2
Nod	NIR	$0\farcs6 \times 11''$	1000–2480	8100		
Stare (P84)	UVB	$5'' \times 11''$	300–600		100k/1pt/hg/2 × 2	100k/1pt/hg/2 × 2
Stare (P85)	UVB				400k/1pt/hg	100k/1pt/hg
Stare (P84)	VIS	$5'' \times 11''$	600–1020		100k/1pt/hg/2 × 2	100k/1pt/hg/2 × 2
Stare (P85)	VIS				400k/1pt/hg	100k/1pt/hg
Stare	NIR	$5'' \times 11''$	1000–2480			

Table 1: X-shooter observing modes for XSL in Periods 84 and 85.

Release Content

The XSL DR1 spectra are reduced, wavelength calibrated, telluric corrected, and relatively flux corrected (we note that due to the "bad weather" observing criterion, absolute flux calibration is not feasible). Where wide slit spectra were available, correction for slit losses is applied (reflected in the **LOSS_COR** header keyword). This release contains 246 observations of 237 stars, covering the full UVB to VIS X-shooter wavelength range.

We show the HRD of these stars as a function of metallicity in Figure 1 and the sky distribution of these stars in Figure 2. Figure 3 shows the DR1 sample stars with calculated stellar parameters (parameters computed using ULySS (Koleva et al. 2009; Wu et al. 2011)) in an HR diagram. Figure 4 shows the distribution of stellar types of these XSL stars.

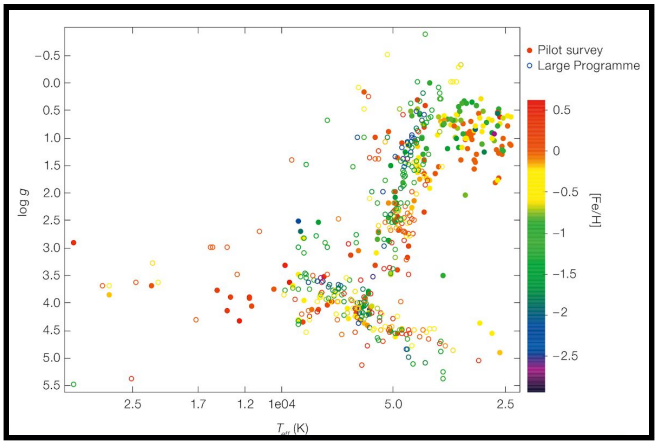

Figure 1: The Hertzsprung–Russell diagram of XSL stars (surface gravity log(g) as a function of effective temperature Teff), colour-coded by metallicity [Fe/H]. The stars of the first data release are indicated by filled circles. The remaining stars are indicated by open circles.

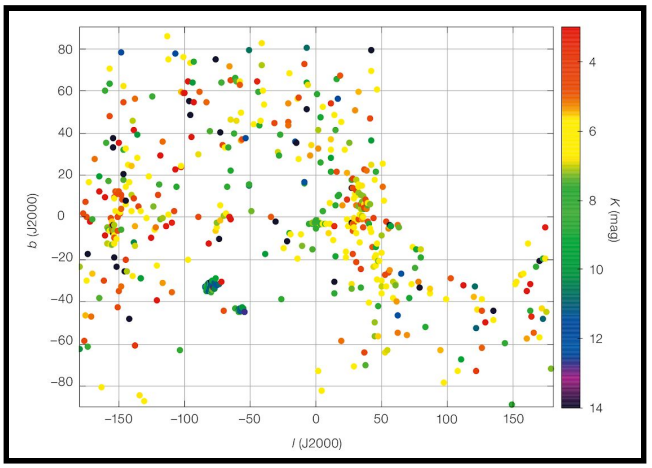

Figure 2: The sky distribution of XSL stars in Galactic coordinates. Points are coloured by their 2MASS K-band magnitudes.

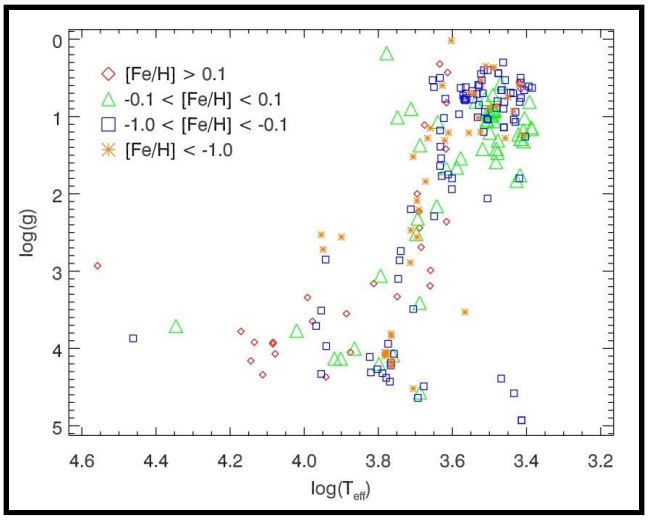

Figure 3: HR diagram of the 219 XSL stars (O–M, LPV, S) with calculated Teff , log(g) and [Fe/H], where [Fe/H] is presented in different colors.

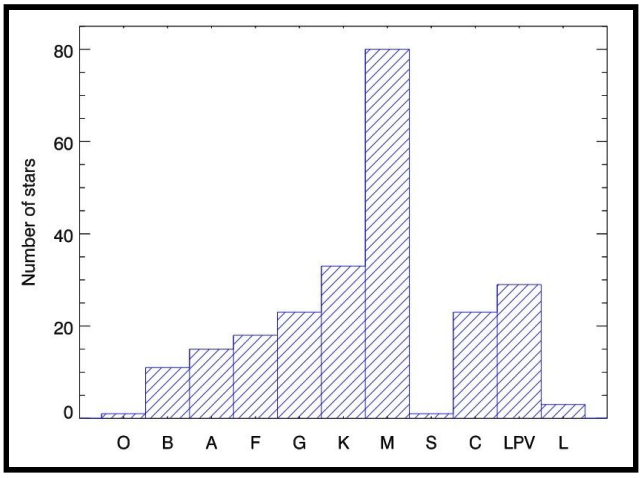

Figure 4: Distribution of spectral types in XSL observed in Periods 84 and 85 (excluding telluric calibrators). Spectral types were retrieved from SIMBAD or based on educated guesses from the source libraries or atmospheric parameters.

We measured the spectral resolution and line shifts of our X-shooter spectra to check the wavelength calibration of our observations. We fitted 212 spectra of F, G, K stars with the synthetic library of Coelho et al. (2005) using the ULySS package (Koleva et al. 2009) to determine the above properties. As shown in Figure 5, the instrumental (velocity) resolution in the UVB arm ranged from 13.3 to 18.1 km/s (velocity dispersion, σ), corresponding to a resolution of 9500–7000. In the VIS arm, the instrumental resolution was constant at 11.6 km/s (i.e., R = 10 986), very close to the resolution of 11 000 given by the X-shooter manuals.

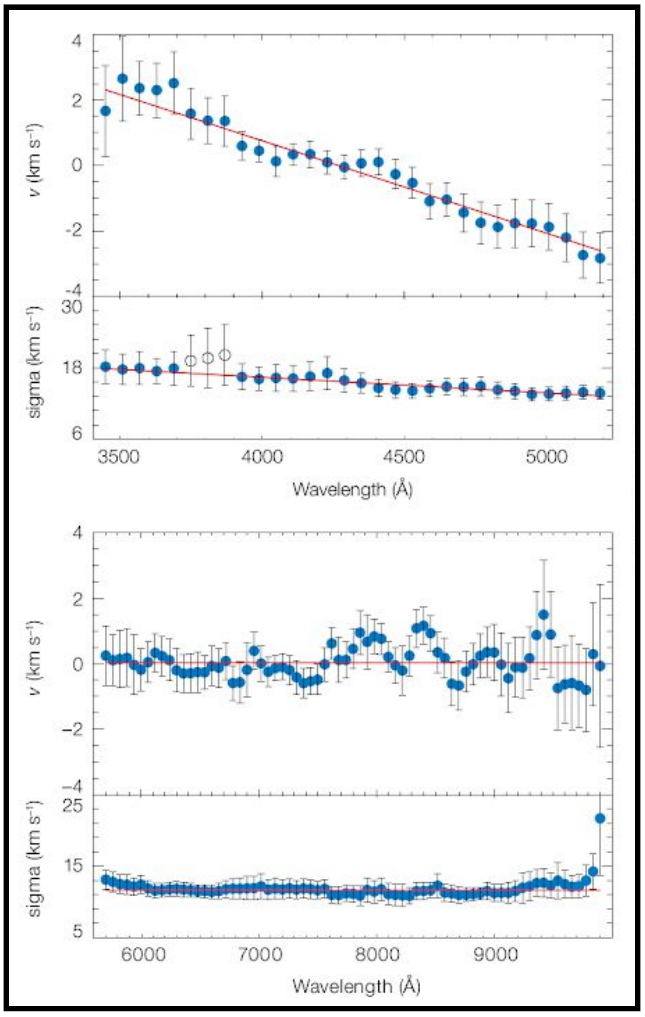

Figure 5: Average line-spread functions for the XSL DR1 FGK stars (212 spectra) in the X-shooter UVB (upper panel) and VIS (lower panel) arms.
In each arm, the top panel shows the residual shift of the spectra (blue dots).
The bottom panel shows the measured instrumental resolution (in velocity units).
The error bars are the standard deviation in each wavelength bin.
A simple first-order polynomial fit (red lines) of the line-spread function is given in each panel.
The three open circles show the region where two different flat-field lamps are used simultaneously in the UVB arm, which may result in larger uncertainties.

Release Notes

Data Reduction and Calibration

The data reduction of the near-ultraviolet and optical spectra from the pilot survey was performed with the public release of the X-shooter pipeline version 1.5.0, following the standard steps described in the X-shooter pipeline manual up to the production of two-dimensional spectra, including bias and/or dark correction, flat-fielding, geometric correction, wavelength calibration and (when necessary) sky subtraction.

Then we extract 1-dimensional (1D) spectra outside of the XSH pipeline to better control the rejection of bad pixels. We further correct the VIS spectra for telluric features using the empirical telluric library of Chen et al. (2014a). This library consists of observations of telluric standard stars with spectral types of B and A from Periods 84 and 85.

After processing all observations in this uniform way, we derive response curves from the flux-standard spectra, and we use these to process both the narrow and wide slit science spectra. Finally, using the wide-slit spectrum corresponding to each narrow slit observation, we derive a wavelength dependent flux-loss correction and apply it to achieve the final XSL spectrum for each stellar observation. This correction was applied to 88% of the current release.

The final DR1 spectra are then shifted to zero velocity and multiple instances of the UVB and VIS spectra are merged into a single spectrum.

XSH Pipeline: Difficulties encountered and proposed solutions

A number of issues were discovered during the pipeline reduction process, which required further processing steps.

Issues with nodding mode observations

Most spectra were reduced using the pipeline recipes that correspond to the observation mode used: spectra observed in staring mode were reduced by the pipeline recipe "xsh_scired_slit_stare", and spectra observed in nodding mode were reduced by the pipeline recipe "xsh_scired_slit_nod".
However, in the case of nodding-mode observations, the first exposure in an A–B pair was occasionally centered in the slit, and the "throw" to the B image (which is fixed angular difference plus a random extra "jitter") was large enough to put the star at the end or even off of the slit in the B image. In these cases, we reduce the well-centered slit in "offset" mode using the second frame as the "sky" frame. This does an excellent job of sky subtraction for these frames, but it means the effective exposure time for these stars is half that anticipated.

Background subtraction issues in UVB spectra

When the sky lines are very weak in stare mode, which is often the case in short-exposure frames, such as in the UVB arm, the background model constructed by the pipeline can fail catastrophically, particularly if weak pattern noise is not properly subtracted by the master bias. This arises from electronic noise from the CCD readout amplifiers and varies in position (and amplitude) on each frame in an unpredictable manner. The derived master bias frame contains

an average of the electronic noise features of each input bias frame, and neither the individual bias frames nor the average master bias frame had the same noise pattern as the science (star) frame. When the pipeline attempts to remove the background ("sky") in the science (star) frame, it generates features in the "sky" that attempt to replicate the noise pattern of the image after correction by the corrupted master bias frame. In such cases, we turn off sky subtraction in the pipeline. Instead, we estimate the sky using pixels on either side of the stellar spectrum in the rectified 2D spectra of each spectrograph order, as would be done for observations in stare mode. The final sky-subtracted 1D spectrum is derived by subtracting the 1D sky spectrum from the 1D spectrum.

Extra cosmic ray cleaning

The X-shooter pipeline (ver. 1.5.0) removes the cosmic ray hits (CRHs) for multiple input images ($n \geq 3$) in nodding and offset modes by computing a median of these images and applying a sigma-clipping. If only two raw images are used as input, as is the case for most of our nodding and offset mode exposures, proper CRH cleaning is not performed by the pipeline. This becomes an issue when a CRH in image "A" is sitting on the same position as the star in image "B"; this results in an artificial emission or absorption line in the final 1D spectrum.
To correct this problem, we use the algorithm of van Dokkum (2001, as implemented in the IDL code "la_cosmic.pro") to clean the raw image before running the pipeline. The CRH-corrected images are then run through the pipeline before extracting the 1D spectrum. The CRH pre-cleaning is used whenever strong CRHs are found to corrupt the 1D spectra.

Bad columns

We have found that the bad pixel maps produced by and used in the pipeline reduction recipes do not always produce a complete list of bad pixels. In particular, a few bad columns in the VIS arm that are improperly mapped in the pipeline disrupt the object spectra in order 26 at 635–638 nm. These bad columns are difficult to correct effectively in the raw spectra and make it difficult to reconstruct the profile of the star in this region. Moreover, due to instrumental flexure, these bad columns can affect different exposures at slightly different wavelengths. In the current version of the spectral library, we have set the fluxes to zero from 635.1 nm to the end of order 26 in the final reduced 2D order-by-order frames.

Extraction of 1D spectra from pipeline-corrected 2D images

After the pipeline reduction and our modifications, we extract a one-dimensional spectrum from the pipeline-corrected, flat-fielded wavelength and geometrically corrected, single-order 2D spectra using our own weighted-extraction code in IDL, which is inspired by the prescription of Horne (1986). There are three extensions in total for each order in the pipeline-produced 2D spectra: the first is the flux in counts, the second is the error, and the third is the quality, which corresponds to the bad pixel mask. We make use of the third extension as the first guess for a bad pixel mask, and the second extension as the square root of each pixel's variance. With 2 to 20 iterations, the bad pixel mask is improved, and most of the CRHs or bad pixels are masked. Spectra from each order are then extracted and merged using a variance-weighted mean of each wavelength in the overlapping regions.

The extraction aperture was set to a fixed width of 4."9 (in narrow-slit observations) or 10."9 (in wide-slit observations) in the optimal-extraction code. However, if significant CRHs or other problems remain within the nominal extraction aperture of the final 2D frame, the extraction aperture was modified to exclude these regions.

We show a G2 star, HD17072, observed in the UVB arm in Fig. 6 to illustrate this process. We note that the orange order between 355 and 370 nm shows noisy features. However, the larger errors in this region yield lower weights compared with the green order in the overlap region. These features therefore do not appear in the final merged spectrum (thin black line).

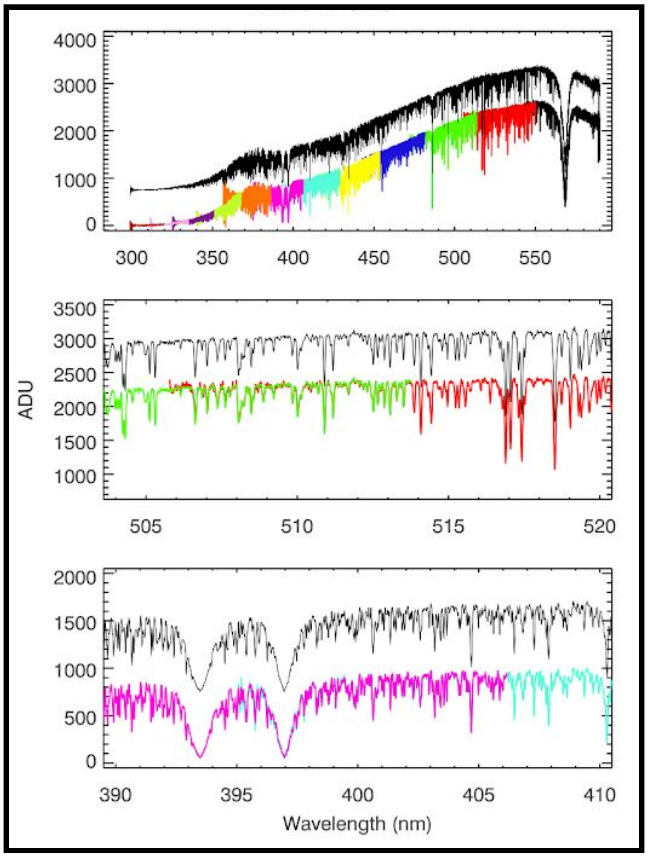

Figure 6: Order-by-order 1D spectrum extraction for the G2 star HD17072 in the UVB arm without flux calibration. Different colors correspond to different orders. The continuous black spectrum is the combined spectrum, which is offset for clarity. In the middle and bottom panels, we zoom in on two wavelength regions, 504–520 nm and 390–410 nm, where orders overlap to see the extraction and combination process in detail.

Saturation

In these first two periods, saturation was a common problem, as our sample contained variable stars near X-shooter's bright target limit (and our exposure times were, in the absence of accurate light curves, determined for the mean stellar brightnesses). Given the large total number of frames in these periods (1847 for the 258 observations, including NIR arm spectra), an automated saturation-detection scheme was required.

Uncorrected CRHs and bad pixels appear as nearly saturated pixels, so a scheme had to be developed to decide which frames were strongly saturated and had to be discarded. Every raw frame was transformed using the following rules. In the UVB and VIS arm images, pixels with counts ≥ 65 000 are set to "1", which means "saturated"; all others are set to "0", which means "good" . Truly saturated frames typically have saturated pixels clustered together in individual orders. We sum each transformed binary "good"/"saturated" image along the wavelength direction for better visualization of the saturation. We show an example of this transformation for a typical saturated raw frame in Fig. 7. Here, saturated pixels are accumulated along the orders, showing sharp features. Raw frames with such features are considered to be "saturated" and removed from the library. In the end, 173 (9.3%) of 1847 extracted spectra were found to be "saturated" and removed.

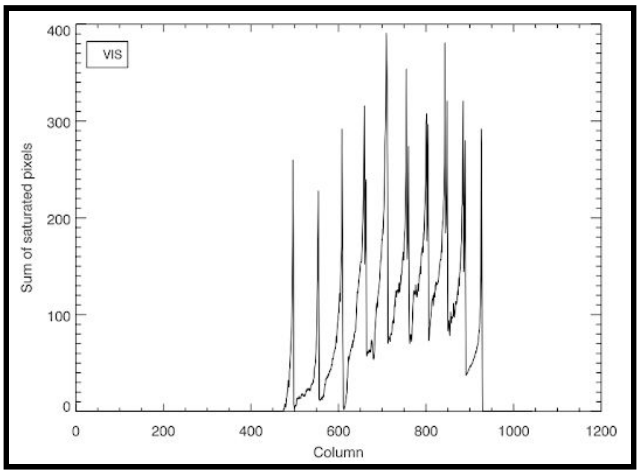

Figure 7: A saturated raw VIS arm frame after transformation of counts to a binary "good pixel"/"saturated pixel" basis, and summed along the wavelength direction. Note the sharp features with values in excess of 200, indicative of saturation due to overexposure.

Telluric absorption correction

Ground-based observations are always subject to contamination from the Earth's atmosphere. In the visible and near-infrared portions of the spectrum, water vapour, molecular oxygen, carbon dioxide and methane generate strong absorption features that originate in the Earth's atmosphere and are referred to as telluric features. Corrections for telluric contamination therefore are important for the XSL spectra in the VIS and NIR arms.

We used "telluric standard star" observations taken as part of the standard X-shooter calibration plan directly after each of our science observations as a basis for telluric correction of our optical data. These stars are typically B2–A0 dwarfs, whose intrinsic spectra contain only H and He absorption lines on top of nearly pure blackbody spectra. We determined the telluric absorption spectrum at the time of observation of each of these stars by dividing the observed spectrum by a model of the star's intrinsic spectrum. We found that the telluric absorption lines changed strength on timescales shorter than the "long" exposure time (> 90 seconds) of faint XSL stars and the total overhead time of ~ 900 seconds, resulting in an imperfect telluric correction. In addition, small changes in spectral resolution and wavelength zero-point occurred even between successive observations. To optimise the telluric correction, we therefore built a library of telluric spectra, in which 152 telluric standard stars were carefully wavelength-calibrated and had their intrinsic spectra modelled and removed.

We developed a principal-component-analysis- (PCA) based method that can quickly and precisely perform telluric corrections for warm stars in XSL. Figure 8 shows the first six principal components from the bottom to top. We found that the first two primary components of our telluric library have a clear physical meaning: the first component presents the mean telluric spectrum of the library; the second component separates the contribution of most of the water vapour features from the O_2 features. We used the first 40 principal components to reconstruct the transmission of each star.

First the science spectrum was normalised, then the reconstructed transmission spectrum was built by projecting the mean-subtracted, normalised science spectrum onto the modified principal components and summing these projections. Telluric correction was finally performed by dividing the spectrum of the programme star by the reconstructed transmission. Figure 9 shows an example of the telluric correction of the K7IV star HD 79349. We found that telluric correction by PCA reconstruction does a good job for both early-type stars and some late-type stars, as this method works better for stars with simpler continua and high signal-to-noise ratios.

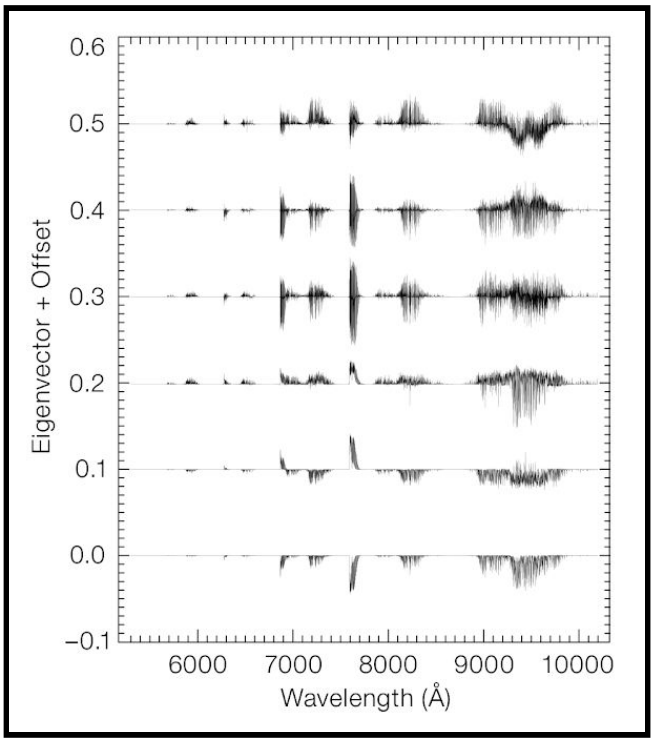

Figure 8: The first six principal components of the telluric library. The eigenvalues decrease from the bottom to the top of this figure (i.e., the first and largest eigenvector is the lowest). The eigenvectors have been offset for display purposes.

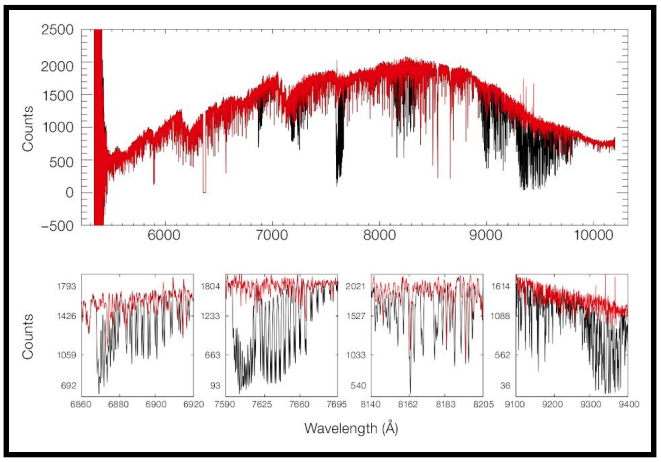

Figure 9: Spectrum of HD 79349 (K7IV) before (black) and after (red) telluric correction in the VIS arm, using the PCA reconstruction method described in the text. The lower panels show four zoomed-in regions to demonstrate the corrections in detail. The spikes around 935 nm are residuals after telluric correction.

Cool stars, such as carbon stars, have strong and sharp molecular bands. Tracing each absorption bandhead to apply the PCA method is therefore difficult for these stars, because some molecular bands occur exactly at the same wavelengths as the telluric absorption regions. Therefore we used the transmission spectrum taken from the telluric library closest in time to the programme star to correct the telluric absorption for all carbon stars, long period variable (LPV) stars and most of the M stars. We show an example of the telluric correction made by both methods on an LPV star OGLEII DIA BUL-SC1 235 in Fig. 10. To make sure where the molecular bands should be, we use an NGSL star HD175865 with similar temperature as a comparison, which has no telluric contamination (as NGSL was observed from space with the *Hubble Space Telescope*).

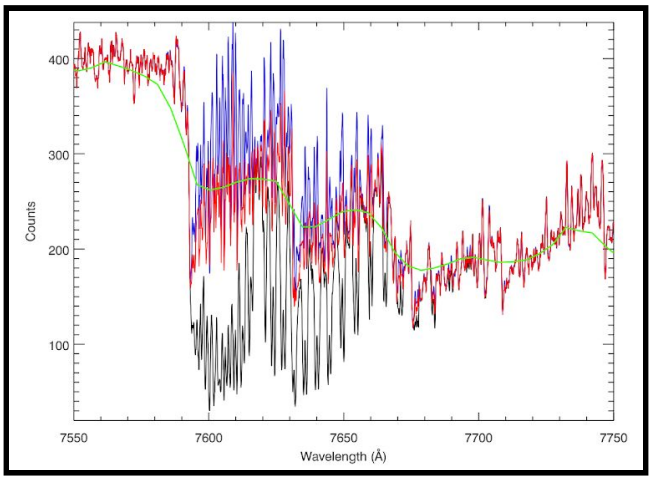

Figure 10: Telluric correction by two different methods for the cool bulge LPV star OGLEII DIA BUL-SC1 235. The black line is the original 1D spectrum extracted, and the blue and red lines are the spectrum after correction by the PCA reconstruction and the temporally-closest telluric absorption spectrum, respectively. The green spectrum is an M5III star with a similar temperature, HD175865, taken from NGSL as a comparison.

Uncertainty of the PCA telluric correction

We have computed the root-mean-squared deviation of the ratio between the PCA-based and closest-in-time telluric corrections for 20 F stars from the sample. We plot this ratio in Fig. 11. We suggest that this is the maximum value of uncertainty that is likely in the PCA-based correction for any given warm star, as the closest-in-time telluric correction could be very different than the true telluric correction, if the closest-in-time calibrator in terms of the timescale of atmospheric changes in the molecular absorption lines was taken at a slightly different airmass at a time that is significantly after the program star.

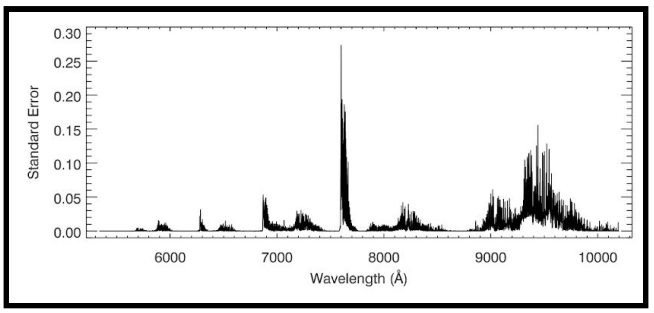

Figure 11: Root-mean-squared deviation of the ratio between the PCA-based and closest-in-time telluric corrections for 20-F stars from XSL.

Flux calibration

Knowledge of the spectral energy distribution of stars allows us to compute synthetic photometry, an important ingredient to compare with catalogues of stellar photometry and to combine stellar spectra together with the correct weights as a function of wavelength in stellar population models. Flux calibration is therefore critical for a spectral library in order to recover the overall spectral energy distribution of each star. Nearly all XSL stars, except the brightest (K < 5 mag), have both narrow-slit observations, to achieve high resolution, and a wide-slit

observation, to preserve the total flux. The brightest stars would have saturated the detectors much too quickly in wide-slit mode and therefore were not observed in this mode.

Construction of the extinction curve

We derived the atmospheric extinction curve of X-shooter in the pilot survey in the UVB and VIS arm using a number of flux-standard stars (BD+17 4708, GD 71, GD 153, EG 274, Feige 110, LTT 3218, and LTT 7987). We reduced and extracted the spectra of flux standard stars with the same set of master bias and master flat-field frames in each arm. Telluric correction was performed in the VIS arm for each flux standard. The spectra of the standards were compared with the flux tables of the appropriate stars from the CALSPEC HST database (Bohlin 2007). By running IRAF.standard and using the Paranal extinction curve (Patat et al. 2011) as a first guess, we derived the extinction curve for our X-shooter observations in the UVB and VIS arms.

The extinction curve of the XSL in Period 84 and 85 is shown in Fig. 12, where the Paranal extinction curve (Patat et al. 2011) is shown as a reference. We find that the inferred extinction curve is very similar to that given by Patat et al. (2011) with a slightly steeper extinction coefficient in the red.

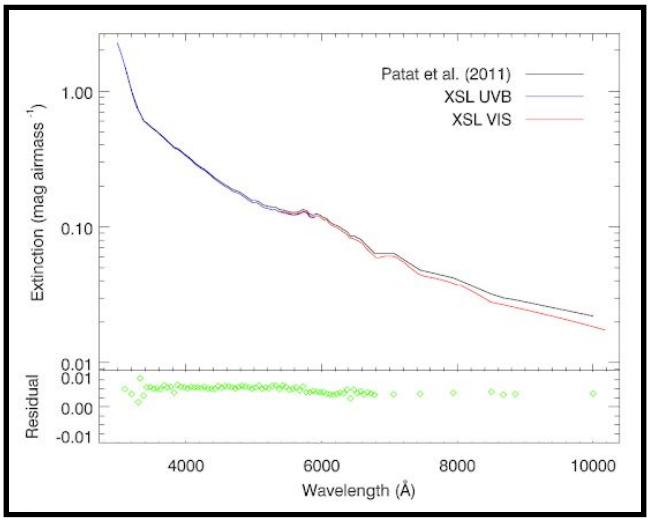

Figure 12: Extinction curve for XSL in the UVB arm (blue line) and the VIS arm (red line). The Paranal extinction curve of Patat et al. (2011) is shown as the black line for comparison. Lower panel shows the residual between XSL and Patat et al. (2011) calculated by the IRAF.standard procedure and applied to derive the XSL extinction

Construction of the response curve

Response curves for individual stars were generated from the chosen flux-standard star observed closest in time.

First, for a given science spectrum, we reduce its flux-standard star with the same set of master bias and master flat-field frames as used for the science observation and extract the 1D spectrum. For the VIS arm spectra, we perform the telluric correction on the 1D spectrum of the flux standard. Second, the airmass of the flux standard is used to derive the atmospheric extinction using the XSL extinction curve. Third, the 1D spectrum of the flux standard is corrected by $F = F_{ADU} / t_{exp} \times AtmExt$, where F_{ADU} is the original 1D spectrum, t_{exp} is the exposure time of the flux standard, and AtmExt is the derived extinction term. We compare this corrected 1D spectrum with its flux table from the CALSPEC HST database. The final response curve is derived by fitting

a spline to the ratio between the reformed 1D flux standard spectrum and the corresponding flux table.

Because the flat field and bias of X-shooter are not stable, at least in Periods 84 and 85, the response curve derived from each flux standard can vary by around 5%. The sharp feature around 3700 Å is due to the two flat field lamps used in the UVB arm. We note that there is a strong feature beyond 5500 Å in the UVB arm. This is due to the dichroic used to split the beam between the UVB and VIS arms.

Flux calibration of individual frames

We note that the dichroic features do not always appear in the same position in the extracted 1D spectra, and therefore, it is difficult to completely remove those features in our final flux-calibrated spectra. To minimize the influence of the dichroic, we choose the observation closest in time for each science observation of a certain flux-standard star as the corresponding flux standard. The chosen flux standard is reduced and extracted as described above. If the binning of the science observation is different from the selected flux standard, we rebin the selected flux standard first.

For each science spectrum, we generated its response curve following the procedure described above. The flux-calibrated science spectrum is derived using the formula,

$$F_{\mathrm{cal,s}}(\lambda) = \frac{F_{\mathrm{ADU,s}}(\lambda)/t^{s}_{\mathrm{exp}}}{\mathrm{Respon} \times \mathrm{AtmExt_s}},$$

where $F_{ADU,S}$ is the 1D spectrum of the science object, t_{exp} the exposure time of the science object, Respon is the derived response curve, and $AtmExt_s$ is the extinction term calculated from the airmass and the extinction curve of XSL. We perform the flux calibration process on both narrow slit and wide slit observations.

Final flux calibration

A final flux calibration is carried out on the narrow-slit observations using the shape of wide-slit observations to avoid flux losses. We use the wide-slit exposure paired with each flux-calibrated, narrow-slit spectrum to do this. If an unsaturated wide-slit observation is available, we run pPXF to shift and broaden the narrow-slit spectrum. The flux correction is performed by multiplying the narrow-slit spectrum by the second-order polynomial determined by pPXF. The **LOSS_COR** keyword is then set to T (True).

For the narrow-slit spectra whose corresponding wide-slit spectrum are saturated, we leave their flux as in the previous step (individual flux calibration). We note that stars without wide-slit flux correction may be missing flux, especially in the UVB arm. The **LOSS_COR** keyword remains set to F (False).

ADC issue in the UVB arm

Some of our data, especially narrow-slit observations in the UVB arm that are observed from 18 July 2010 to 2 August 2010, are influenced by a failure of the atmospheric dispersion compensator (ADC). To correct for this ADC issue, we perform the following steps. First, we run pPXF to determine the possible shift and broadening between the narrow- and wide-slit observations. Second, we convolve the narrow-slit observation to the same resolution and wavelength range as the wide-slit exposure according to the first step. Third, we smooth the wide-slit observation and wide-slit-like narrow slit spectrum, respectively, with a boxcar size of 500 pixels to avoid possible noise features. The final compensation curve is given by the ratio of

smoothed versions of the wide- and narrow-slit observations. Once the compensation curve is derived, we multiply it to the original narrow-slit spectrum to perform the flux calibration.

Rest-frame velocity correction and Arm combination

After carefully checking the resolution and flux calibration of our sample, we shift every spectra to zero velocity using the synthetic libraries of Coelho et al. (2005); Palacios et al. (2010), and Allard et al. (2011) as templates. The second wavelength calibration in the UVB arm is carefully performed to correct the small shifts shown in the upper panel of Fig. 5. Multiple observations of the same non-variable star are combined in the same arm. Multiple observations of the same variable star are kept as different spectra.

We merge multiple UVB and VIS arm spectra of each star into a single spectrum using the overlapped region, mostly from 5420 to 5650 Å. Some of the spectra have the dichroic features slightly shifted in wavelength, and in this case, we shift the overlapped regions accordingly. The merged spectra of each star are carefully checked and evaluated to maintain the appropriate spectral shape.

Data Quality

The current data release consists of data products with a basic quality assurance process. We made sure that they satisfy two main criteria: homogeneity of the data reduction process and a thorough visual inspection of the final products.

Synthetic photometry comparison

We calculated synthetic colours on the Johnson–Cousins UVBRI and Sloan Digital Sky Survey (SDSS) photometric systems for the XSL stars and compared these colours with published values to check the reliability of our flux calibration. By comparing the calculated synthetic B–V, U–B, R–I, and V–I colours of the XSL-sample with the NGSL library (Gregg et al., 2006) [see Figure 13 and Table 2 below] and observed colours from the Bright Star Catalogue (Hoffleit et al., 1983; Hoffleit & Jaschek, 1991) [see Figure 14 and Table 3 below], we found good agreement between XSL sample and literature stars, with offsets < 0.02 mag in all colours and scatters ranging from 0.07 mag in U–B to 0.02 mag in R–I.

	(U-B)	(B-V)	(R-I)	(V-I)
XSL - NGSL	-0.017	-0.002	0.008	-0.006
rms	0.071	0.046	0.024	0.049

Table 2: Mean color difference and rms scatter between XSL and NGSL.

	(B-V)	(U-B)
XSL - BSC	-0.024	0.016
rms	0.058	0.080

Table 3: Mean color difference and rms scatter between XSL and the Bright Star Catalogue (BSC).

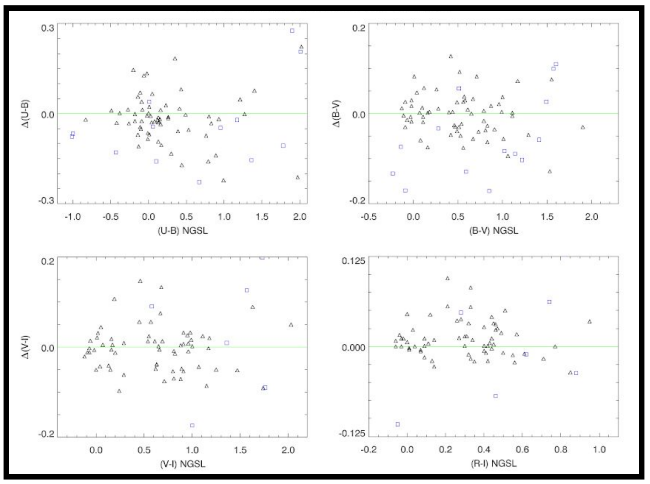

Figure 13: Comparison of synthetic (U − B), (B − V), (V − I), and (R − I) colors in XSL and NGSL. The residuals in each panel are calculated as color XSL − color NGSL . Blue squares indicate those stars that likely have flux losses, due to a lack of useful wide-slit observation.

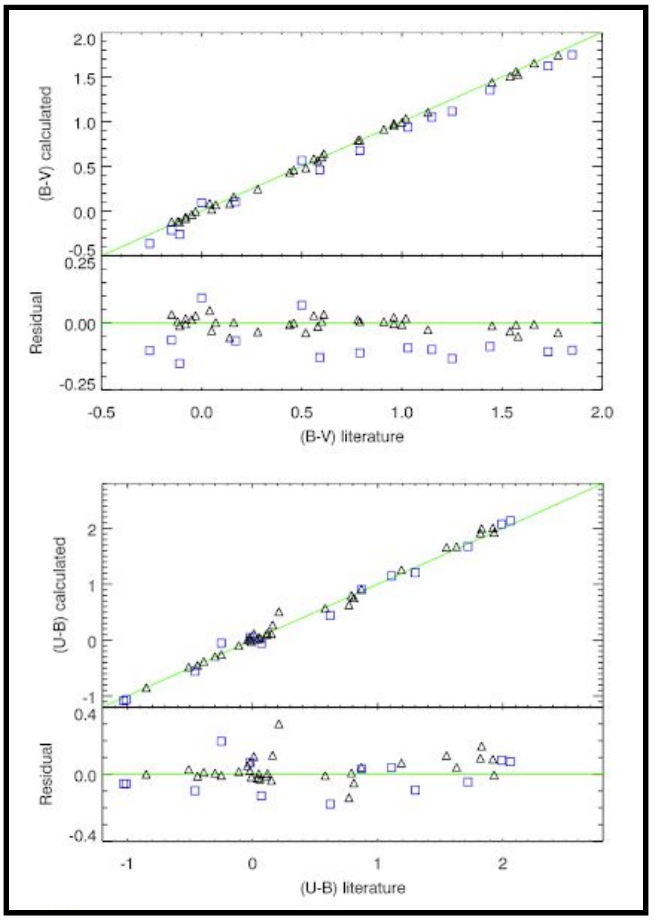

Figure 14: Comparison of synthetic (B − V) and (U − B) colors of XSL and the Bright Star Catalogue. The residuals are calculated as in Fig. 13. Blue squares indicate those stars that likely have flux losses due to a lack of useful wide-slit observation.

Since there are few literature stars which have SDSS colors in common with our sample, we use the model colors computed by Lenz et al. (1998) as a rough check. Models with log(g) = 4.5 and log(g) = 2.5 are chosen to represent the main sequence and giants, respectively. Three metallicities [M/H] = −2.0, 0, and 1.0 are used to cover the metallicity range of the XSL sample. Figure 15 shows the u'−g' vs g'−r' colors and r'−i' vs g'−r' colors for the XSL sample compared with the model colors. In general, the agreement between the models and data is very good. The coolest model from Lenz et al. has T eff = 3500 K, which is significantly warmer than the coolest XSL stars, and so the reddest model colors are not as red as the reddest XSL stars.

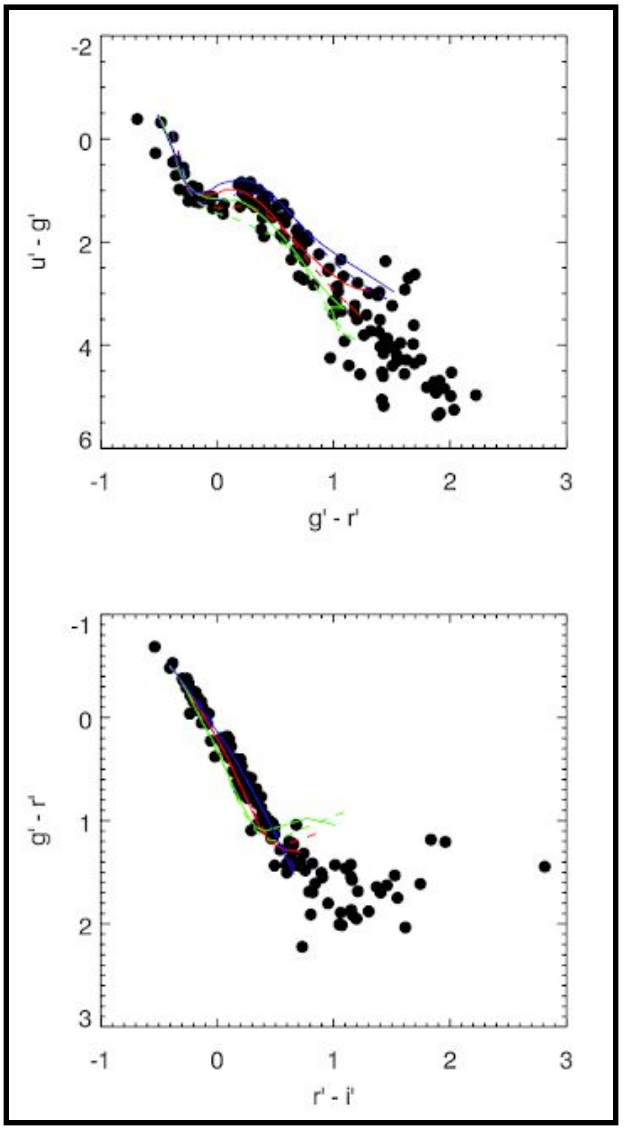

Figure 15: Synthetic SDSS colors of the XSL sample (black dots) compared with synthetic model colors by Lenz et al. (1998). Only three metallicities are shown for the model colors: [M/H] = −2.0 (blue lines), 0.0 (red lines), and +1.0 (green lines). Solid lines indicate models with log(g) = 4.5 and dashed lines indicate models with log(g) = 2.5.

Comparison with literature spectra

As a further check, we made a direct comparison of the final XSL spectra with other libraries. The first year of XSL (DR1) had 77 stars in common with NGSL, 40 stars in common with the MILES (Sánchez-Blázquez et al., 2006) stellar spectral library, 34 stars in common with the ELODIE (Prugniel & Soubiran, 2001, 2004; Prugniel et al., 2007) spectral library, 26 stars in common with

the IRTF (Rayner et al., 2009) spectral library and 25 stars in common with the CaT (Cenarro et al., 2001) spectral library. For each comparison, we convolved the comparison spectrum and XSL to the same intrinsic resolution, matched the continua, and measured the fractional difference between these spectra in telluric-free regions.

We show several examples of the spectral slope comparison between XSL, NGSL, MILES and CaT in Fig 16.

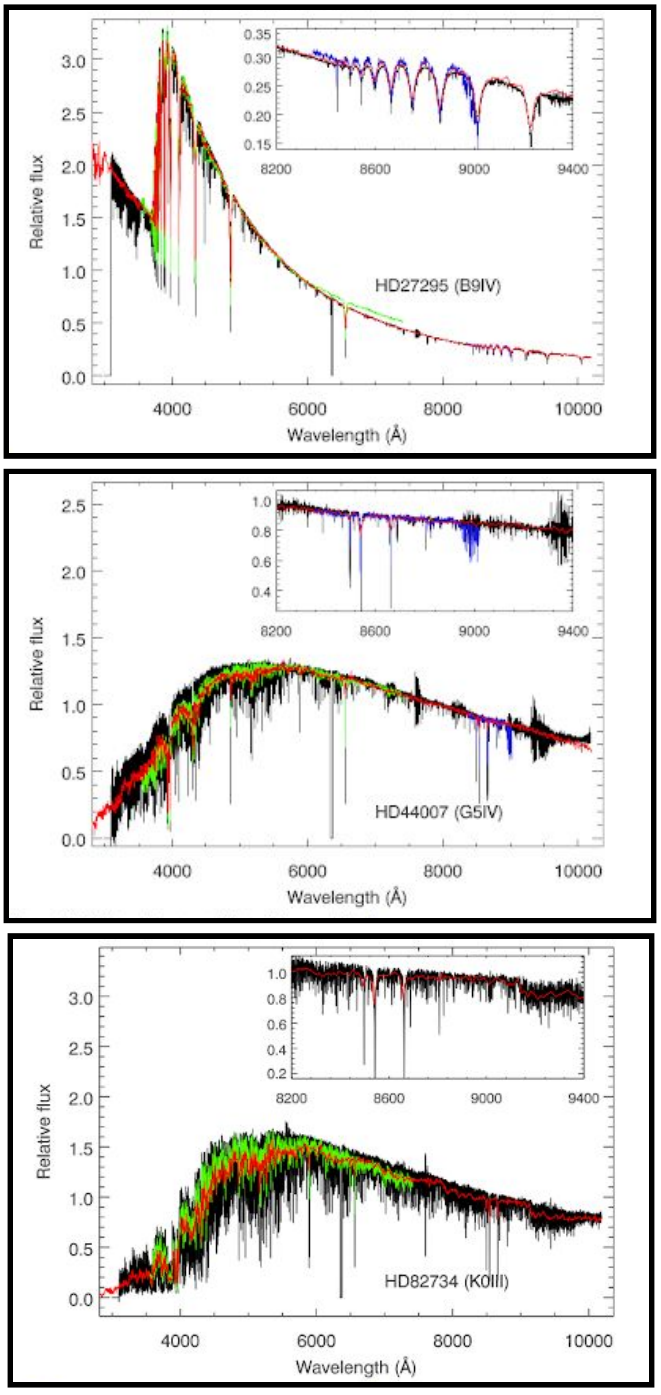

Figure 16: Spectra of HD27295 (top), HD 44007 (middle) and HD 82734 (bottom) from XSL (black). The corresponding spectra from other spectral libraries are indicated in green for MILES, red for, NGSL, and blue for CaT. The inset shows a zoomed-in region for a detailed comparison of the telluric corrections.

Comparing the XSL spectra with two higher-resolution spectral libraries, UVES POP (Bagnulo et al., 2003) and ELODIE, we found that the typical residual between XSL and UVES POP is 2–4% in relative flux after convolving the UVES POP spectra to the XSL resolution, and the typical residual between XSL and ELODIE is 2–6% in relative flux after similarly convolving ELODIE to the XSL resolution. We found very good agreement in the line shapes and depths between XSL and the two higher-resolution libraries for both warm and cool stars. Comparison of XSL with the intermediate-resolution spectral library MIUSCAT (a combination of MILES, Indo–U.S. and CaT; Vazdekis et al., 2012) showed a typical flux residual between XSL and MIUSCAT of 2%. Figures 17 to 19 show the results of these comparisons.

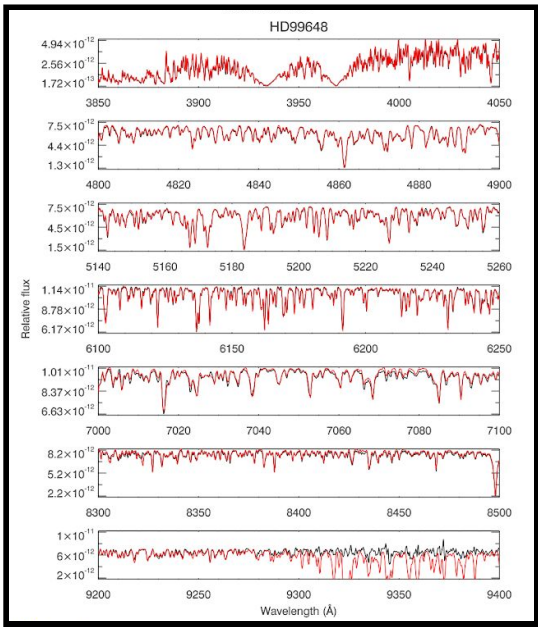

Figure 17: Detailed spectral line comparison between XSL (black) and UVES-POP (red) of HD 99648 (G8Iab), where the UVES-POP spectrum is smoothed to the resolution of XSL. Telluric features are clearly seen in the UVES-POP spectrum, especially around 9300–9400 Å

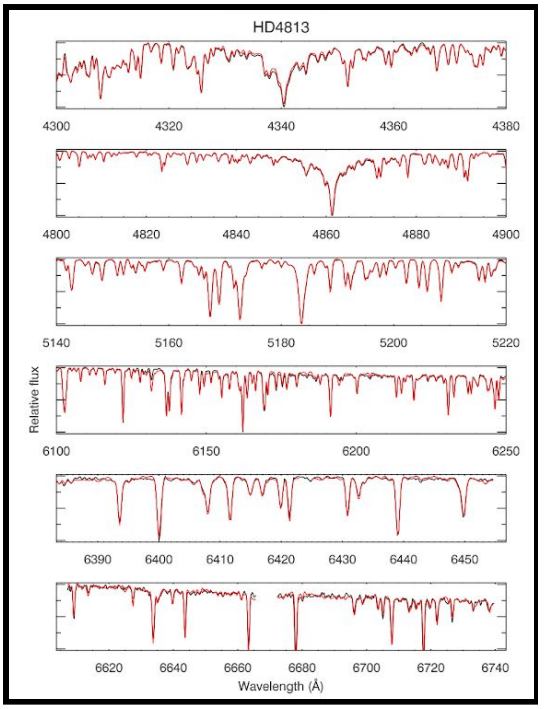

Figure 18: Detailed spectral line comparison between XSL (black) and ELODIE (red) of HD 4813 (F7IV-V), where the ELODIE spectrum is smoothed to the resolution of XSL. The gap in the two bottom panels represents bad pixels in ELODIE.

Comparison of XSL with the lower-resolution spectral library NGSL also showed good agreement: the typical relative flux residual between XSL and NGSL was 1% over the common wavelength 320–1000 nm after removing the continuum shapes, as seen in Figure 20.

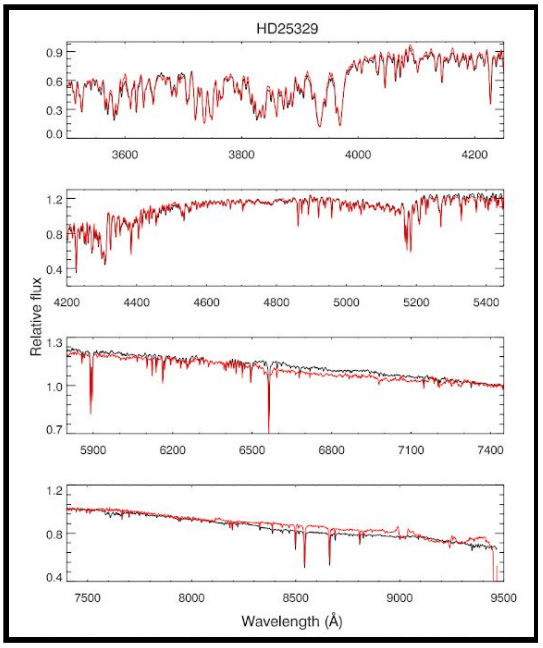

Figure 19: Detailed spectral line comparison between XSL (black) and MIUSCAT (red) of HD 25329 (K1V), where the XSL spectrum is smoothed to the resolution of MIUSCAT. The gap in the third panel represents bad pixels in XSL.

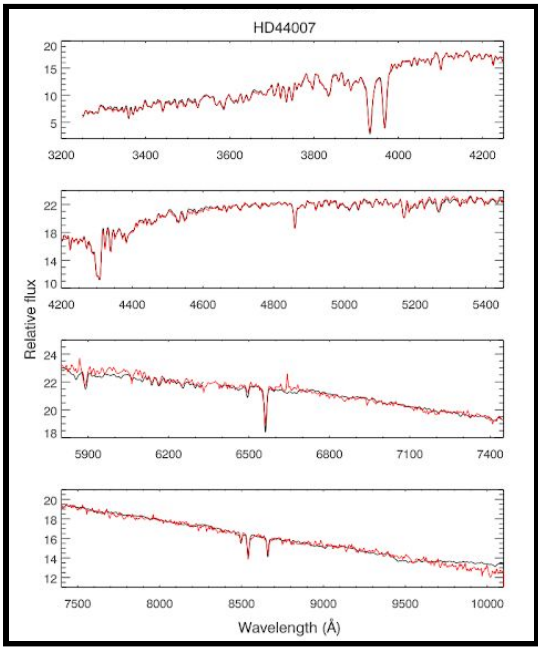

Figure 20: Detailed spectral line comparison between XSL (black) and NGSL (red) of HD 44007 (G5IV:w...), where the XSL spectrum is smoothed to the resolution of NGSL. The gap in the third panel represents bad pixels in XSL.

Known issues

The errors related to the correction for telluric absorption are not included in the error spectrum, and about 10% of the error spectra are erroneous, in the sense that their level is obviously too high by a factor of 10 or more.

For some stars, the slit-loss correction was not performed, due to a missing wide-slit observation. Check the **LOSS_COR** header keyword and examine Table B1 from Chen et al. (2014a) for more details.

Data Format

Files Types

The XSL DR1 spectra are merged spectra, with linearly sampled wavelengths in rest-frame, covering the wavelength range 300–1020 nm. The spectra are provided as FITS binary tables, each containing three columns:

1. WAVE: Wavelength [in nm].
2. FLUX: Flux spectrum [in erg/s/cm^2/Å]
3. ERR: Error spectrum: [same units as Flux]

WAVELMIN and WAVELMAX are ESO keywords that describe the minimum and maximum wavelengths in nanometers outside of which the described spectrum does not carry any valuable scientific information. In our case, WAVELMIN and WAVELMAX were defined as the first and last wavelengths where mean(FLUX)/standard_deviation(FLUX) > 0.2.

Acknowledgements

Please cite Chen et al. 2014a (2014A&A...565A.117C) and Chen et al 2014b (2014Msngr.158...30C), when using these data.

Based on data products created from observations collected at the European Organisation for Astronomical Research in the Southern Hemisphere under ESO programme(s) 084.B-0869, 085.B-0751 and 189.B-0925 (PI Trager).

This research has made use of the services of the ESO Science Archive Facility.